Hot fusion-evaporation cross sections of ^{45}Sc-induced reactions with lanthanide targets

T. A. Werke,[1,2] D. A. Mayorov,[1,2] M. C. Alfonso,[1,2] M. E. Bennett,[1,*] M. J. DeVanzo,[1,3,†] M. M. Frey,[1,2,‡] E. E. Tereshatov,[1] and C. M. Folden III[1,‖]

[1]*Cyclotron Institute, Texas A&M University, College Station, Texas 77843, USA*

[2]*Department of Chemistry, Texas A&M University, College Station, Texas 77843, USA*

[3]*Department of Physics, Astronomy and Geosciences, Towson University, Towson, Maryland 21252, USA*

(Received 21 May 2015; revised manuscript received 11 August 2015; published 22 September 2015)

Background: ^{45}Sc has rarely been studied as a projectile in fusion-evaporation reactions. The synthesis of new superheavy elements with $Z > 118$ will require projectiles with $Z > 20$, and ^{45}Sc could potentially be used for this purpose.

Purpose: Cross sections were measured for the xn and pxn exit channels in the reactions of ^{45}Sc with lanthanide targets for comparison to previous measurements of ^{48}Ca reacting with similar targets. These data provide insight on the survival of spherical, shell-stabilized nuclei against fission, and could have implications for the discovery of new superheavy elements.

Methods: Beams of $^{45}Sc^{6+}$ were delivered from the K500 superconducting cyclotron at Texas A&M University with an energy of ≈5 MeV/nucleon. Products were purified using the Momentum Achromat Recoil Spectrometer, and excitation functions were measured for reactions of ^{45}Sc + $^{156-158,160}$Gd, ^{159}Tb, and ^{162}Dy at five or more energies each. Evaporation residues were identified by their characteristic α-decay energies. Experimental data were compared to a simple theoretical model to study each step in the fusion-evaporation process.

Results: The maximum measured $4n$ cross sections for the reactions ^{45}Sc + $^{156-158,160}$Gd, ^{159}Tb, and ^{162}Dy are $5.8 \pm 1.7, 25 \pm 5, 39 \pm 7, 150 \pm 20, 2.4^{+2.3}_{-1.4}$, and 1.8 ± 0.6 μb, respectively. Proton emission competes effectively with neutron emission from the excited compound nucleus in most cases. The α, αn, and $\alpha 2n$ products were also observed in the ^{45}Sc + ^{162}Dy reaction.

Conclusions: Excitation functions were reported for ^{45}Sc-induced reactions on lanthanide targets for the first time, and these cross sections are much smaller than for ^{48}Ca-induced reactions on the same targets. The relative neutron-deficiency of the compound nuclei leads to significantly increased fissility and large reductions in the survival probability. Little evidence for improved production cross sections due to shell-stabilization was observed.

DOI: 10.1103/PhysRevC.92.034613 PACS number(s): 25.70.Gh, 25.70.Jj

I. INTRODUCTION

Nuclides near the $Z = 82$, $N = 126$ closed shells have a broad range of deformations, nucleon binding energies, and fissilities, and are an interesting test region for the study of fusion-evaporation residue (EvR) cross sections. Several publications have focused on the production of neutron-deficient compound nuclei (CN) with $Z = 83-87$ [1–5] and comparisons of the experimental data with model calculations. Various models [6–13] have been proposed to reproduce EvR cross sections by adjusting parameters such as the fission barrier height or including phenomena such as collective enhancements [14] and fission dissipation [15]; however, there is still no consensus on how to best reproduce the experimental data. Andreyev *et al.* produced neutron-deficient isotopes of Bi [1], Po [1], and At [2] and observed significant contributions from pxn evaporation channels that competed effectively with the xn channels. A large (≈ 30%) reduction in the theoretical fission barrier was needed to accurately reproduce the experimental data using the code HIVAP. Sahm *et al.* [3] and Vermeulen *et al.* [4] studied the production of actinide nuclides on and near the $N = 126$ spherical closed shell but did not observe the expected increase in EvR cross sections due to stabilizing ground-state shell effects. More recently, we reported similar findings in the bombardment of lanthanide targets with ^{48}Ca projectiles, where large yields of the weakly deformed xn evaporation channels but weak contributions from pxn channels were observed [5]. Reactions with ^{45}Sc ($Z = 21$) projectiles have been largely ignored as a candidate for heavy-ion fusion-evaporation reactions and very little literature data exists. These reactions are expected to have lower fusion probabilities than reactions with ^{48}Ca projectiles due to a larger Coulomb repulsion. Additionally, the relative neutron-deficiency of ^{45}Sc compared to ^{48}Ca leads to higher neutron binding energies, lower fission barriers in the CN, and reduced survival probabilities of the CN. These tendencies are expected to be exacerbated by collective enhancements to level density (CELD), where the large number of rotational and vibration levels at the fission saddle-point lead to increases in the fission probability of the CN [14]. CELD can result in a substantial decrease of the EvR cross section for the production of spherical nuclei near closed shells, which are principally

*Present address: Nuclear Engineering Division, Argonne National Laboratory, Argonne, IL 60439 USA.

†Present address: Lockheed Martin Space Systems Company, King of Prussia, PA 19406 USA.

‡Present address: Lower Colorado River Authority, Austin, TX 78744 USA.

‖Corresponding author: Folden@comp.tamu.edu

susceptible to this effect due to a lack of rotational levels in the ground state.

The reactions of ^{45}Sc projectiles with ^{159}Tb, ^{162}Dy, and $^{156-158,160}$Gd targets to form CN near the $Z = 82$, $N = 126$ closed shells have been studied in the current work. To the best of the authors' knowledge, this work represents the first reported EvR cross sections for ^{45}Sc-induced hot fusion-evaporation reactions with lanthanide targets. The targets were selected to cover CN with $Z = 85-87$ and to examine the isotopic influence of the target on the production cross section. The xn and pxn channels were observed in nearly all cases, and the α, αn, and $\alpha 2n$ channels were observed with the ^{162}Dy target only. These reactions are part of a systematic study of reactions of $Z \geqslant 20$ projectiles with lanthanide targets, and preliminary results were reported in Ref. [16]. The current ^{45}Sc data are interpreted using a simple theoretical model aimed at elucidating the major effects that determine the EvR cross sections. The nuclei studied in this work span a range of deformations and should help to clarify the influence of CELD. The current work is especially important in the context of recent experiments on the production of new, spherical superheavy elements (SHEs) up to $Z = 118$ in ^{48}Ca-induced reactions with actinide targets up to ^{249}Cf ($Z = 98$). (See the review in Ref. [17] and references therein.) Unfortunately, future element discovery experiments may require projectiles with $Z > 20$, since targets with $Z > 98$ are not sufficiently available. ^{45}Sc has been considered as a projectile for SHE synthesis [18,19], but no experiments of this type have been performed so far. This work provides an unprecedented quantitative comment on the potential of ^{45}Sc in SHE research.

II. EXPERIMENTAL METHODS

Experiments were performed at the Cyclotron Institute at Texas A&M University. The list of reactions is given in Table I along with properties of each CN. Beams of $^{45}Sc^{6+}$ were delivered from the K500 cyclotron with a kinetic energy of $\approx$5 MeV/nucleon and with intensities on-target of 0.5−8.0 pnA. Targets of ^{159}Tb (479 μg/cm^2, self-supporting), ^{162}Dy (403 μg/cm^2 on 75 μg/cm^2 ^{nat}C), $^{160}Gd_2O_3$ (655 μg/cm^2 on 2 μm Ti), $^{158}Gd_2O_3$ (680 μg/cm^2 on 2 μm Ti), $^{157}Gd_2O_3$ (405 μg/cm^2 on 2 μm Ti), and $^{156}Gd_2O_3$ (479 μg/cm^2 on 2 μm Ti) were irradiated in three temporally separated experiments. The ^{159}Tb target was purchased from Microfoils Co., and the ^{162}Dy target was prepared by vacuum deposition on ^{nat}C at Lawrence Berkeley National Laboratory. The Gd_2O_3 targets were prepared on-site by molecular plating the desired nitrate salt onto the Ti backing and baking under atmospheric conditions at 200 °C for 30–60 min to convert the material to the oxide form [20,21]. The beam dose on target was monitored online with a pair of circularly collimated (1 or 2 mm collimator diameter) Si monitor detectors positioned in the plane of the beam and offset by ±30° from the beam axis. In preparatory experiments, substantial backgrounds were observed in the spectra, so an additional cylindrical plastic "blocker" 21.6 mm in length with a 6.35 mm diameter opening was positioned in front of each collimator and carefully aligned to the target center in order to further reduce the number of unwanted scattered particles entering the detector. The absolute beam dose was calibrated using an electron-suppressed Faraday cup located in the target chamber.

The Momentum Achromat Recoil Spectrometer (MARS) [22,23] was used to purify the beam of reaction products. It has been previously characterized for heavy recoils, and the experimental setup in the current work was substantially similar to that described in Ref. [24]. The primary beam energy from the cyclotron was determined by passing the beam through a 48 μg/cm^2 ^{nat}C foil and measuring the magnetic rigidity of the resultant charge states through the first MARS dipole magnet. Beam energies for the excitation function measurements were varied using Al degraders of 0 (no degrader), 1.2, 2.25, 2.85, 3.45, 4.5, 5.1, and 6.29 μm thickness. All energy loss calculations were performed using the SRIM Stopping and Range Tables [25,26] as implemented in LISE++ [27]. The desired reaction products were tuned through MARS by estimating the most probable charge state in LISE++ using the method of Schiwietz and Grande [28]. The efficiency of MARS has been previously determined to be (3.5 ± 0.7)% and (2.2 ± 0.5)% for the ^{40}Ar + ^{118}Sn, ^{165}Ho reactions, respectively [5,24]. A linear interpolation of the mass asymmetry parameter $\eta = |A_p - A_t|/(A_p + A_t)$ was used to give efficiencies in the range of (2.7 ± 0.6)% to (2.8 ± 0.6)%, and the efficiency was assumed to be constant

TABLE I. Properties of the ^{45}Sc-induced reactions studied in the current work. N_{CN} represents the neutron number of the CN. Z_1Z_2 is the charge product of the reaction. $\overline{B_f - S_n}$ is the average difference in fission barrier and neutron separation energy during the $4n$ deexcitation cascade. Fission barriers in this table are calculated for $l_{CN} = 0$ using the rotating finite-range liquid drop model of Sierk [51] with shell corrections taken from Möller *et al.* [45]. S_p(CN) and S_n(CN) are the proton and neutron separation energies of the CN, respectively, taken from Ref. [31]. $\beta_2(CN)$ is the quadrupole deformation of the CN taken from Ref. [45].

Reaction	CN	N_{CN}	Z_1Z_2	$\overline{B_f - S_n}$ (MeV)	S_p(CN) (MeV)	S_n(CN) (MeV)	β_2(CN)
^{45}Sc+^{156}Gd	^{201}At	116	1,344	−0.2	1.124(17)	9.87(3)	+0.071
^{45}Sc+^{157}Gd	^{202}At	117	1,344	+0.8	1.350(30)	7.87(3)	+0.062
^{45}Sc+^{158}Gd	^{203}At	118	1,344	+1.8	1.527(18)	9.64(3)	+0.045
^{45}Sc+^{160}Gd	^{205}At	120	1,344	+4.0	1.918(19)	9.17(3)	+0.035
^{45}Sc+^{159}Tb	^{204}Rn	118	1,365	−0.2	3.109(18)	9.90(3)	−0.087
^{45}Sc+^{162}Dy	^{207}Fr	120	1,386	0.0	1.018(23)	9.67(3)	−0.104

for the xn and pxn exit channels. For the αxn exit channels, the transmission efficiency is smaller due to the larger angular distribution after α-emission. Using the code TERS 2.0 [29,30], the transmission efficiency was estimated to be a factor of 7 smaller for the αxn channels.

Reaction products that reached the detector chamber implanted into a 50 mm × 50 mm Micron model X1 position-sensitive silicon detector (PSSD). The PSSD had 16 position-sensitive vertical strips and a full-energy signal with a FWHM of ≈70−80 keV. Calibration of the full-energy signal was performed using a four-peak α-particle source purchased from Eckert & Ziegler containing ≈10 nCi each of ^{148}Gd, ^{239}Pu, ^{241}Am, and ^{244}Cm. The vertical position calibration was performed with an aluminum mask with six slits 1 mm wide and separated by 8 mm. The correction for the recoiling daughter energy of the implanted EvRs was calibrated using products of the ^{45}Sc + ^{106}Pd (587 μg/cm^2, self-supporting) reaction. The geometric efficiency of the PSSD was estimated to be (55 ± 3)% for α particles emitted into the detector. The fraction of the EvR distribution that struck the PSSD was estimated to be ≈(100 ± 2)% in the horizontal direction and ≈(95 ± 5)% in the vertical direction based on the observed distribution of implanting events.

Alpha decays were discriminated from implantation events via a large-area microchannel plate (MCP) detector purchased from Photonis, Inc. Incoming ions passed through a 0.6 μm Al foil and ejected secondary electrons, which were steered onto the plates of the MCP by an electrostatic grid. The low-resolution MCP energy signal was amplified and recorded in the same manner as a Si detector, but was not used as a trigger due to excess electronic noise. Coincident signals in the PSSD and MCP indicated a recoil event, while a signal only in the PSSD indicated alpha decays. The PSSD trigger was used as a start signal and a delayed MCP signal was used as a stop signal for a time-to-amplitude converter. Recoil events were separated from alpha decays with an efficiency of > 99% as determined in offline tests using fission fragments from a ^{252}Cf source. Live-time measurements and time-stamping of events were provided by a 1 MHz clock generator purchased from Stanford Research Systems.

III. EXPERIMENTAL RESULTS

The ^{45}Sc projectile energies were chosen such that the production of the 4n product would be maximized as is common in "hot fusion" experiments. Fusion-evaporation products were identified by their characteristic alpha decay energies [31] in the PSSD, and Table II gives the decay properties of the expected 4n and $p3n$ reaction products. Spectra were prepared containing events discriminated by the MCP veto detector and examples are shown in Fig. 1. Peaks of interest were fit using the GF3 program in the RADWARE software package [32], and the measured alpha energies (also given in Table II) show good agreement with the literature data.

Many of the observed fusion-evaporation channels were near the limits of experimental sensitivity due to small cross sections and/or low α branching ratios. To determine which data were above background, a simple statistical test similar to that described in Ref. [33] was used. The number of average background counts per bin $N_{\rm bkgd}$ was measured by fitting a flat background to that region of the spectrum using GF3, and a region of interest (ROI) based on the detector resolution was selected. The expected number of *background* counts μ in the ROI was calculated by multiplying $N_{\rm bkgd}$ by the bin width of the ROI. The Poisson probability of observing y background counts when μ are expected is $P(y|\mu) = \mu^y e^{-\mu}/y!$. The data were accepted to be above background with confidence level $\varepsilon = 95\%$ if the actual number of counts was greater than or equal to n, the smallest integer which makes the following inequality true:

$$\sum_{j=0}^{n} P(j|\mu) = \sum_{j=0}^{n} \frac{\mu^j}{j!} e^{-\mu} \geqslant \varepsilon. \qquad (1)$$

In other words, a peak was considered above background only if the number of counts was greater than the 95% confidence limit of a cumulative Poisson distribution of background counts.

If a peak passed the statistical test described above, then a cross section for the corresponding exit channel was calculated using the background-subtracted number of counts.

TABLE II. Decay properties of the 4n and $p3n$ evaporation residues produced in the current work. $E_{\alpha,\,\rm obs}$ is the measured α energy. Ground state decays were not observed in some cases. Literature values are taken from Ref. [31]. Error bars are not available for the branching ratios in some cases.

Reaction	4n, $p3n$ EvRs	$E_{\alpha,\rm obs}$ (keV)	$E_{\alpha,\rm lit}$ (keV)	$b_{\alpha,\rm lit}$ (%)	$t_{1/2,\rm lit}$
^{45}Sc+^{156}Gd	^{197}At	6960 ± 12	6959.0 ± 3.0	100	0.388 ± 0.006 s
	^{197}Po	6326 ± 27	6281.0 ± 4.0	44 ± 7	53.6 ± 1.0 s
^{45}Sc+^{157}Gd	^{198}At	6724 ± 26	6753.0 ± 4.0	97	4.1 ± 0.3 s
	^{198}Po	6184 ± 49	6182.0 ± 2.2	57 ± 2	1.77 ± 0.03 min
^{45}Sc+^{158}Gd	^{199}At	6620 ± 31	6643.0 ± 3.0	90	7.03 ± 0.15 s
	^{199m}Po	6030 ± 10	6059.0 ± 3.0	39 ± 4	4.17 ± 0.05 min
^{45}Sc+^{160}Gd	^{201}At	6314 ± 31	6342.0 ± 1.0	59	83 ± 2 s
	^{201m}Po	5766 ± 33	5786.0 ± 2.0	2.9 ± 0.3	8.9 ± 0.2 min
^{45}Sc+^{159}Tb	^{200}Rn	6874 ± 16	6902.0 ± 3.0	98	0.96 ± 0.03 s
	^{200m}At	6386 ± 52	6411.8 ± 1.3	57	43 ± 1 s
^{45}Sc+^{162}Dy	^{203}Fr	7072 ± 27	7131.0 ± 5.0	95	0.549 ± 0.015 s
	^{203m}Rn	6580 ± 29	6550.3 ± 1.0	78	26.9 ± 0.5 s

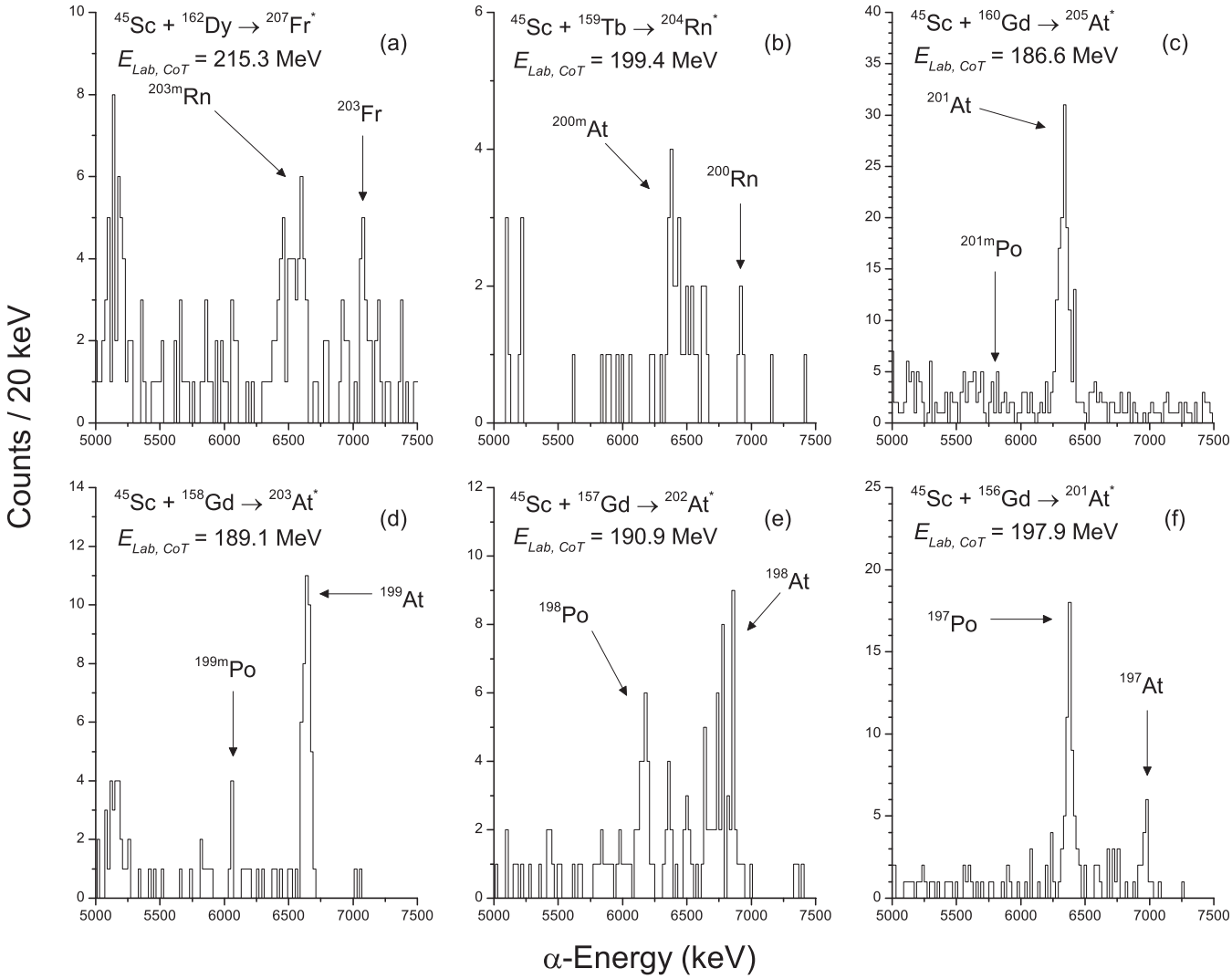

FIG. 1. Alpha spectra observed in the indicated irradiations. $E_{\mathrm{Lab,\,CoT}}$ is the laboratory frame projectile energy at the center of the respective targets. The indicated projectile energies correspond to the peak of the 4*n* excitation functions. The expected locations of the 4*n* and *p*3*n* products are labeled; the ^{201m}Po peak indicated in panel (c) did not pass the statistical test described in Sec. III.

Approximately half of all possible "peaks" were rejected by the test. Electron capture decay of *xn* products can increase the amount of *pxn* products in the detector, so corrections were made using the known branching ratios. The luminosity in each experiment was measured based on the observed count rate in the monitor detectors and the known scattering cross section. A full listing of measured cross section data for all observed exit channels is given in Table III. The associated errors are statistical only; due to uncertainties primarily from the transmission efficiency of MARS, absolute uncertainties are estimated to be ±50%. All reported errors are calculated at the 1σ level, with symmetric error bars reported for channels with sufficient statistics ($\geqslant$ 15 counts after background subtraction), and asymmetric error bars reported for channels with low statistics [33].

The data for the 4*n* and *p*3*n* reactions are plotted in Fig. 2, since these are the channels most likely to be populated when the projectile energy is just above the Coulomb barrier. The 4*n* data fall largely along the expected qualitative trends. The series of Gd targets provides an opportunity to observe the effect of changing the neutron number of the target, and ^{160}Gd has the largest peak cross section (150 ± 20 μb) while ^{156}Gd has the smallest (5.8 ± 1.7 μb). While it was not surprising that the ^{159}Tb target had a smaller peak 4*n* cross section than the ^{158}Gd target, it was surprising that the decrease was greater than one order of magnitude ($2.4^{+2.3}_{-1.4}$ μb compared to 39 ± 7 μb, respectively). The addition of a single proton to the target resulted in a substantial decrease in cross section, and suggests that the combination of an odd-*Z* projectile bombarding an odd-*Z* target is not favorable. Only one data point from the ^{45}Sc + ^{162}Dy reaction passed the statistical test. Together, the peak 4*n* cross sections span two orders of magnitude, corresponding to the change in target from ^{160}Gd to ^{162}Dy. This change represents an addition of only two protons, but has a substantial impact on the survival of the compound nucleus and the final EvR cross sections. (See the discussion in Sec. V).

Excitation functions were also measured for many *pxn* channels. The data show that *pxn* exit channels competed

TABLE III. List of measured evaporation residue cross sections. $E_{\mathrm{Lab,\,CoT}}$ is the center-of-target projectile energy in the laboratory frame, and E^*_{CN} is the corresponding CN excitation energy. Reported cross sections are only for those data that passed the statistical test described in Sec. III. Some of these data are also presented in Figs. 2 and 3.

Target	$E_{\mathrm{Lab,CoT}}$(MeV)	E^*_{CN} (MeV)	σ_{3n} (μb)	σ_{4n} (μb)	σ_{5n} (μb)	σ_{6n} (μb)	σ_{p2n} (μb)	σ_{p3n} (μb)	σ_{p4n} (μb)	σ_{p5n} (μb)
^{156}Gd	182.6	38.9	5.8 ± 1.7	$1.2^{+0.9}_{-0.6}$			$3.6^{+1.9}_{-1.3}$	$1.4^{+1.1}_{-0.7}$		
	191.5	45.8	$3.1^{+1.9}_{-1.3}$	$3.4^{+1.8}_{-1.3}$				26 ± 5		
	197.9	50.8		5.7 ± 2.1				32 ± 5		
	203.3	54.9						24 ± 5	13 ± 3	
	208.7	59.1						11 ± 3	34 ± 5	
^{157}Gd	185.3	42.7	$9.8^{+4.6}_{-3.4}$							
	190.9	47.1	$6.7^{+3.1}_{-2.3}$	25 ± 5				18 ± 6	$5.9^{+3.2}_{-2.3}$	
	194.2	49.6	14 ± 4	22 ± 5			36^{+21}_{-15}	$8.0^{+3.9}_{-2.9}$		
	198.2	52.7	$2.9^{+2.4}_{-1.5}$	20 ± 5				39 ± 8	18 ± 5	
	200.5	54.5	$3.7^{+2.3}_{-1.6}$	14 ± 4	$3.5^{+2.1}_{-1.5}$		49^{+25}_{-18}	42 ± 8	28 ± 6	
	205.9	58.7		$3.3^{+2.9}_{-1.8}$				15 ± 6	29 ± 7	
	211.3	62.9						10^{+6}_{-4}	42 ± 9	$6.9^{+4.0}_{-2.8}$
^{158}Gd	180.4	40.8	15^{+13}_{-8}	$7.1^{+6.8}_{-4.3}$			69^{+59}_{-38}			
	185.9	45.1	$8.7^{+6.2}_{-4.2}$	34 ± 8						
	189.1	47.6	$8.3^{+5.2}_{-3.7}$	39 ± 7				26^{+24}_{-15}		
	195.3	52.4		33 ± 5	$3.0^{+1.9}_{-1.3}$			17^{+15}_{-9}	$3.5^{+2.6}_{-1.7}$	
	201.3	57.1		17 ± 4	11 ± 4			88 ± 33	23 ± 7	
^{160}Gd	181.2	45.4		100 ± 20						
	186.6	49.6	41 ± 14	150 ± 20	35 ± 10					
	189.9	52.2		120 ± 20	100 ± 20			150^{+120}_{-80}		
	194.3	55.6	12^{+6}_{-4}	140 ± 10	140 ± 10	$2.4^{+1.4}_{-1.0}$			38^{+15}_{-11}	
	202.0	61.1		28 ± 9	330 ± 30	41 ± 7				55^{+30}_{-22}
^{159}Tb	195.0	49.4					$4.8^{+4.1}_{-2.6}$			
	195.8	50.0						40 ± 14		
	199.4	52.8		$2.4^{+2.3}_{-1.4}$				39 ± 10	$3.1^{+2.5}_{-1.6}$	
	201.2	54.2						26 ± 10	$3.0^{+2.5}_{-1.6}$	
	203.9	56.3		$0.8^{+0.6}_{-0.4}$	$0.5^{+0.4}_{-0.3}$		9.8 ± 2.3	52 ± 5	9.5 ± 1.4	
	205.8	57.8					$7.4^{+3.3}_{-2.5}$	54 ± 8	17 ± 3	
	213.3	63.6		$2.0^{+1.3}_{-0.9}$			$8.1^{+3.4}_{-2.6}$	31 ± 6		
	217.0	66.5						19 ± 6	29 ± 4	
	221.4	69.9							11^{+6}_{-4}	15^{+7}_{-5}
^{162}Dy	201.5	51.3					$1.1^{+0.6}_{-0.4}$	8.1 ± 1.6	$1.1^{+0.6}_{-0.5}$	
	206.0	54.8					$1.2^{+0.9}_{-0.6}$	8.7 ± 2.4	$2.2^{+1.3}_{-0.9}$	
	207.7	56.2					$1.3^{+0.7}_{-0.5}$	10 ± 2	6.6 ± 1.5	
	215.3	62.1	$1.2^{+0.8}_{-0.5}$	1.8 ± 0.6	$0.7^{+0.4}_{-0.3}$		2.5 ± 0.8	7.2 ± 1.6	3.6 ± 1.0	
	218.9	64.9					$0.8^{+0.5}_{-0.3}$	$1.6^{+0.8}_{-0.6}$	12 ± 2	$0.7^{+0.4}_{-0.3}$
	223.3	68.3							6.6 ± 1.2	2.4 ± 0.6
			σ_{α}(μb)	$\sigma_{\alpha n}$(μb)	$\sigma_{\alpha 2n}$(μb)					
^{162}Dy (cont.)	201.5	51.3	98^{+40}_{-31}							
	206.0	54.8								
	207.7	56.2	200 ± 60	35^{+17}_{-12}						
	215.3	62.1	40^{+30}_{-20}							
	218.9	64.9		88 ± 20	$6.6^{+5.1}_{-3.3}$					
	223.3	68.3		79 ± 18	29 ± 8					

effectively with the xn products that are most commonly reported in hot fusion reactions. For the more neutron-rich systems, the xn cross sections are greater than the associated pxn cross sections (i.e., $4n$ vs $p3n$) as shown in Fig. 2. As the systems become more neutron-deficient, the pxn cross sections remain relatively constant while the xn cross sections decrease dramatically. The maximum $p3n$ cross sections for the reactions with Gd targets are 150^{+120}_{-80} μb, 88 ± 33 μb, 42 ± 8 μb, and 32 ± 5 μb from most neutron-rich to most neutron-poor. It should be noted that $^{201\mathrm{m}}$Po is the $p3n$ EvR of the ^{45}Sc + ^{160}Gd reaction and has a small alpha branch (2.9%), so a small statistical fluctuation in the number of counts can potentially lead to an unexpectedly large cross section. (The ground state product ^{201g}Po was not observed in this reaction).

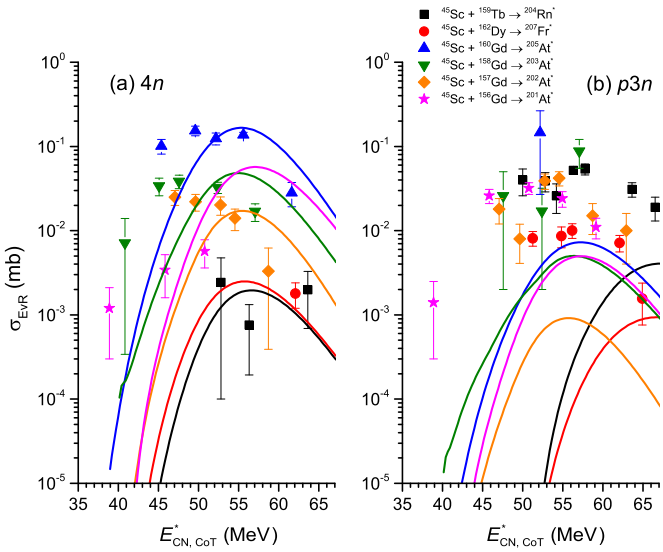

FIG. 2. (Color online) Measured excitation functions for the (a) $4n$ and (b) $p3n$ reactions studied in the present work. Symbols represent measured data and solid lines indicate calculations according to the model described in Sec. IV. The symbols are the same on both panels. These data are also presented in Table III.

All of the other points of the ^{160}Gd(^{45}Sc, $p3n$)^{201m}Po excitation function did not pass the statistical test described in Sec. III, and 1σ upper limits are $< 80\,\mu$b. The ^{45}Sc + ^{159}Tb reaction is notable because both reaction partners are odd Z. The peak $p3n$ cross section ($54 \pm 8\,\mu$b) is a factor of ≈20 larger than the peak $4n$ cross section ($2.4^{+2.3}_{-1.4}\,\mu$b), suggesting that the presence of loosely bound protons in the projectile and target increases the likelihood of proton emission, but the current work was not able to investigate this phenomenon in detail.

Additionally, the α, αn, and $\alpha 2n$ channels were observed in the ^{45}Sc + ^{162}Dy reaction, and the cross sections were significantly larger than for the corresponding xn and pxn channels. The CN in this reaction has the highest Coulomb energy and Q_α of any CN in the current work, which likely contributed to the emission of alpha particles. According to Eq. (14) below, the alpha emission barrier is greater than 18 MeV, so the emitted alpha particles should have taken away a large fraction of all available excitation energy. The high kinetic energies create a large phase space, also making emission more likely. The data suggest that the use of neutron-deficient projectiles to produce heavy elements is not promising, since some of the total EvR cross section will contribute to αxn channels.

IV. MODEL CALCULATIONS

We have developed a simple theoretical model to help understand the measured EvR excitation functions. A similar model was described in our previous publication to explain the measured xn cross sections of ^{48}Ca-induced reactions with lanthanide targets [5]. In that work, good agreement with the data was achieved while considering only neutron emission and fission competition from the excited CN. Table III shows that the production of pxn and other charged-particle emission channels was substantial in the current work, so modifications have been made to include charged-particle exit channels when calculating the survival of the CN.

The cross section for EvR production $\sigma_{\rm EvR}$ is typically modeled as the product of the capture cross section $\sigma_{\rm capt}$, the compound nucleus formation probability $P_{\rm CN}$, and the probability of the compound nucleus surviving against fission $W_{\rm sur}$:

$$\sigma_{\rm EvR}(E_{\rm cm},\ l) = \sigma_{\rm capt}(E_{\rm cm},l) \times P_{\rm CN}(E_{\rm cm},\ l) \times W_{\rm sur}(E^*_{\rm CN},\ l_{\rm CN}), \quad (2)$$

where $E_{\rm cm}$ is the kinetic energy of the projectile in the center-of-mass frame, $l_{\rm CN}$ is the angular momentum of the CN, and $E^*_{\rm CN}$ is the excitation energy of the CN. $\sigma_{\rm capt}$ was calculated using the "diffused barrier formula" proposed by Świątecki *et al.* [12] and details are described by Eqs. (2) through (8) in Ref. [5].

Quasifission has been shown to reduce $P_{\rm CN}$ below 1 in reaction systems of heavy ions on deformed targets with charge products as small as $Z_1Z_2 \approx 540$–1000 [34–38]. Values of Z_1Z_2 are given in Table I and are much greater than 1000, so it is expected that quasifission will moderately hinder the fusion probabilities for these reactions. No experimental data have been measured for $P_{\rm CN}$ in reactions of ^{45}Sc projectiles on any targets; thus, we can only make predictions based on our knowledge of $P_{\rm CN}$ values that have been measured in similar reactions, such as ^{48}Ca-induced reactions with the deformed lanthanide targets ^{154}Sm and ^{168,170}Er [39,40]. $P_{\rm CN}$ was measured or deduced to be ≈0.3−0.8 for these ^{48}Ca-induced reactions. To first order, one would expect the values of $P_{\rm CN}$ in ^{45}Sc-induced reactions to be slightly smaller than those in ^{48}Ca-induced reactions *on the same targets* due to the slightly larger charge product of the projectile-target system. $P_{\rm CN}$ has been modeled based on a semiempirical formula proposed by Siwek-Wilczynska *et al.* [41]:

$$P_{\rm CN} = \zeta \times 10^{-(z/b)^k}, \quad (3)$$

where ζ is a scaling factor, $z = Z_1Z_2/(A_1^{1/3} + A_2^{1/3})$, $k \approx 3.0$, and $b = 2(E_{\rm cm} - B)/{\rm MeV} + 135$ (see the discussion surrounding Eq. (10) in Ref. [5]). In this work, ζ was chosen to be 2.5 to be consistent with our previous work, and typical values of $P_{\rm CN}$ for these ^{45}Sc-induced reactions on deformed lanthanide targets are calculated to be ≈0.1 for $E^*_{\rm CN} \approx 50$ MeV. It should be noted that $P_{\rm CN}$ is the least well understood part of the fusion-evaporation mechanism [42], and the error associated with the $P_{\rm CN}$ calculation can be up to an order of magnitude. However, the values calculated here are reasonable estimates for the reaction systems under study.

Calculating the survival probability of an excited compound nucleus against fission has been treated as a statistical problem due to the large level density of the excited CN. The general expression for the survival probability of an excited CN is given as

$$W_{\rm sur} = P_{xn}(U_{\rm CN}) \prod_{j=1}^{x} (\Gamma_n/\Gamma_{\rm tot})_j, \quad (4)$$

where $\Gamma_n/\Gamma_{\rm tot}$ is the ratio of the neutron decay width Γ_n to the total decay width ($\Gamma_{\rm tot} = \Gamma_f + \Gamma_n + \Gamma_p + \Gamma_\alpha$) for the jth step in the deexcitation process, and $P_{xn}(U_{\rm CN})$ is the so-called "Jackson factor" [43] that defines the probability of emitting exactly x neutrons given an initial compound nucleus with "thermal energy" $U_{\rm CN}$ (defined below).

Each decay width was calculated independently following the prescription of Siwek-Wilczyńska *et al.* [13,44]. In the Fermi-gas approximation, the decay widths for particle emission and fission are given respectively as

$$\Gamma_i = \frac{K_{{\rm coll},\,i}\, g_i m_i \sigma_i U_i}{\pi^2 \hbar^2 a_i} \exp[2(a_i U_i)^{1/2} - 2(a_0 U_0)^{1/2}], \quad (5)$$

$$\Gamma_f = \frac{2K_{{\rm coll},\,f}[(a_f U_f)^{1/2} - 1]}{4\pi a_f} \times \exp[2(a_f U_f)^{1/2} - 2(a_0 U_0)^{1/2}], \quad (6)$$

where g_i is the spin degeneracy of emitted particle i, m_i is its mass, σ_i is the cross section for the inverse reaction, a_i is the level density parameter after emission of particle i, a_0 is the level density parameter of the parent nucleus, a_f is the level density parameter of the parent nucleus at the fission saddle point, and the other quantities are defined below. The thermal energy of the parent nucleus U_0, the thermal excitation energy available for particle emission U_i, and the thermal energy for fission U_f are

$$U_0 = E^*_{\rm CN} - E_{{\rm rot},\,0} - P_0, \quad (7)$$

$$U_i = E^*_{\rm CN} - E_{{\rm rot},\,i} - S_i - B_i - P_i, \quad (8)$$

$$U_f = E^*_{\rm CN} - E_{{\rm rot,\,saddle}} - B_f - P_{\rm saddle}, \quad (9)$$

where $E_{\rm rot}$ is the respective rotational energy, P is the respective pairing energy (discussed below), S_i is the separation energy of particle i, B_i is the barrier for emission of particle i, and B_f is the fission barrier height. The experimental separation energies S_i were taken from Ref. [31]. The rigid body rotational energies were used as suggested in [9,13,14] and are given by $E_{\rm rot} = J(J+1)\hbar^2/2I$, where J is the angular momentum quantum number, $I = (2/5)m_0 A R^2(1 + \beta_2/3)$, $m_0 = 931.494\,{\rm MeV}/^2$, $R = (1.2\,{\rm fm})A^{1/3}$, and β_2 is the quadrupole deformation parameter taken from Ref. [45].

The asymptotic level density parameter was calculated using the prescription of Reisdorf (see Eq. (5) in Ref. [6]):

$$\tilde{a}/{\rm MeV}^{-1} = 0.04543(r_0/{\rm fm})^3 A + 0.1355(r_0/{\rm fm})^2 A^{2/3} B_S + 0.1426(r_0/{\rm fm})A^{1/3} B_K, \quad (10)$$

where $r_0 = 1.15\,{\rm fm}$ and B_S and B_K are the surface and curvature factors, respectively. B_S and B_K are taken from the rotating liquid drop model, and values are tabulated in Ref. [46]. Note that $B_S = B_K = 1$ for spherical nuclei. The specific level density parameters are modified for shell effects following Ignatyuk *et al.* [47]:

$$a_i = \tilde{a}\left\{1 + \frac{\delta S^{A-A_i}}{U_i}[1 - \exp(-U_i/E_D)]\right\}, \quad (11)$$

$$a_f = \tilde{a}\left\{1 + \frac{\delta S^{A}_{\rm saddle}}{U_f}[1 - \exp(-U_f/E_D)]\right\}. \quad (12)$$

The shell corrections δS^{A-A_i} and $\delta S^A_{\rm saddle}$ are for the particle emission daughter and parent fission saddle point, respectively, and $E_{\rm D} = 18.5\,{\rm MeV}$ is the shell damping parameter. The shell correction at the fission saddle is negligible ($\delta S^A_{\rm saddle} \approx 0$), so $a_f \approx \tilde{a}$ [13].

It has been shown that the barrier for charged-particle emission from an excited, rotating nucleus is reduced due to shape polarization effects [48,49]. The proton and alpha particle emission barriers B_p and B_α, respectively, are calculated using the functions proposed by Parker *et al.* from experimentally measured barriers over a wide range of excited nuclei [50]:

$$B_p/{\rm MeV} = 0.106Z - 0.9, \quad (13)$$

$$B_\alpha/{\rm MeV} = \frac{2.88(Z-2)}{1.470(A-4)^{1/3} + 4.642}. \quad (14)$$

Calculated barriers for proton emission from this method are ≈40% smaller than would be expected from a touching spheres configuration. The macroscopic component of the fission barrier is calculated using the rotating finite-range liquid drop model of Sierk [51] with reductions due to angular momentum (described below) using the FISROT code [52]. The microscopic shell correction is adopted from the tabulated data of Möller *et al.* [45]. Average values of $l_{\rm CN}$ were calculated using the coupled-channel code CCFULL [53], but only small impact parameters and thus small angular momenta should contribute to the EvR cross sections because the higher partial waves result in almost certain fission during the deexcitation cascade. Previous work has suggested limits of $\approx 25\hbar$ for Bi nuclei [1] and $\approx 20\hbar$ for ^{220}Th [54] produced in similar reactions. Therefore, $l_{\rm CN}$ was limited to 40% of the CCFULL estimate or $25\hbar$ (whichever was lower). Each neutron, proton, and alpha particle was assumed to carry away $2\hbar$, $3\hbar$, and $10\hbar$ of angular momentum when emitted, respectively, based on Ref. [55].

Pairing energies were assumed to be $(22\,{\rm MeV})/A^{1/2}$ for even-even, $(11\,{\rm MeV})/A^{1/2}$ for even-odd or odd-even, and zero for odd-odd nuclei. The pairing energy at the saddle point was assumed to be the same as the pairing energy of the ground state. The temperature of the excited CN was recalculated at each step of the deexcitation process, and was assumed to be $T = (U_0/a_0)^{1/2}$, where

$$a_0 = \tilde{a}\left\{1 + \frac{\delta S^A}{U_0}[1 - \exp(-U_0/E_D)]\right\}, \quad (15)$$

and δS^A is the shell correction energy of the parent nucleus. The neutron kinetic energy was assumed to be $\varepsilon_n = T$, which corresponds to the most probable energy of a quasi-Maxwellian distribution. The proton kinetic energies are described by a Coulomb-shifted quasi-Maxwellian distribution [56,57], so the proton kinetic energy was assumed to be $\varepsilon_p = B_p + T$.

The inclusion of CELD was necessary to reproduce data for the ^{48}Ca-induced reactions in Ref. [5], so this effect is included in the current model. The level density enhancement factor

$K_{\mathrm{coll},\,i}$ for each decay mode (including fission) is calculated following the prescription of Zagrebaev *et al.* [9] using a smoothing function ϕ and the Fermi function f to account for the fade-out of collective effects as excitation energy increases:

$$K_{\mathrm{coll},\,i}(U_i,\,\beta_2) = [K_{\mathrm{rot},\,i}\,\phi(\beta_2) + K_{\mathrm{vib},\,i}\,\phi(1-\beta_2)]f(U_i), \tag{16}$$

$$\phi(\beta_2) = \left[1 + \exp\left(\frac{\beta_2^0 - |\beta_2|}{\Delta\beta_2}\right)\right]^{-1}, \tag{17}$$

$$f(U_i) = \left[1 + \exp\left(\frac{U_i - E_{\mathrm{crit}}}{d_{\mathrm{crit}}}\right)\right]^{-1}, \tag{18}$$

where $\beta_2^0 \approx 0.15$, $\Delta\beta_2 \approx 0.04$, $E_{\mathrm{crit}} = 40$ MeV, and $d_{\mathrm{crit}} = 10$ MeV. For particle emission, β_2 was taken to be the ground-state value tabulated by Möller *et al.* [45], while for fission, β_2 was taken to be the saddle point value from Cohen and Świątecki [58]. The rotational and vibrational enhancement factors K_{rot} and K_{vib}, respectively, are

$$K_{\mathrm{rot}} = IT/\hbar^2, \tag{19}$$

$$K_{\mathrm{vib}} = \exp\left[0.0555A^{2/3}(T/\mathrm{MeV})^{4/3}\right]. \tag{20}$$

$K_{\mathrm{rot}} \approx 100-150$ is typically an order of magnitude greater than $K_{\mathrm{vib}} \approx 1-10$ due to the smaller level spacing of rotational bands.

V. DISCUSSION

As a test of the model described in Sec. IV, we performed calculations for $4n$ reactions of ^{45}Sc + ^{160}Gd, ^{159}Tb (reported in the current work), ^{48}Ca + ^{159}Tb (reported in Ref. [5]), ^{40}Ar+^{159}Tb (reported in Ref. [4]), and ^{40}Ca+^{159}Tb (reported in Ref. [2]), and results are presented in Fig. 3. The reported ^{48}Ca and ^{40}Ar xn cross sections are substantially larger than the ^{45}Sc and ^{40}Ca xn cross sections, so this provides a test of the model's ability to reproduce data over several orders of magnitude (greater than the expected influence of CELD). The ^{40}Ar +^{165} Ho reaction leads to the same CN as the ^{45}Sc + ^{160}Gd reaction and should test how well our model calculates σ_{capt} and P_{CN}, as W_{sur} should ideally be the same in both cases. As shown in Fig. 3, the difference in the product $\sigma_{\mathrm{capt}}P_{\mathrm{CN}}$ accounts for nearly all of the difference in the $4n$ EvR cross sections between the two reactions. For $E^*_{\mathrm{CN}} \approx 50$ MeV, the ratio of the measured $4n$ cross sections in the ^{40}Ar +^{165} Ho reaction and the ^{45}Sc + ^{160}Gd reaction is $\sigma_{4n}(^{40}\mathrm{Ar})/\sigma_{4n}(^{45}\mathrm{Sc}) \approx 73 \pm 16$. The calculated difference in $4n$ cross section due to the entrance channel at this excitation energy for these two reactions is $\sigma_{\mathrm{capt}}P_{\mathrm{CN}}(^{40}\mathrm{Ar})/\sigma_{\mathrm{capt}}P_{\mathrm{CN}}(^{45}\mathrm{Sc}) \approx 69$. This suggests that the model calculations give reasonable values for σ_{capt} and P_{CN}. Unfortunately, the production of pxn channels in the ^{48}Ca- and ^{40}Ar-induced reactions was not significant [4,5], so charged-particle decay widths are not well tested by this procedure. Regardless, the agreement with the experimental $4n$ data is very good. Model calculations are also presented in Fig. 2 as solid lines.

Our model calculations generally agree well with the measured data for the $4n$ exit channel [see Figs. 2(a) and 3],

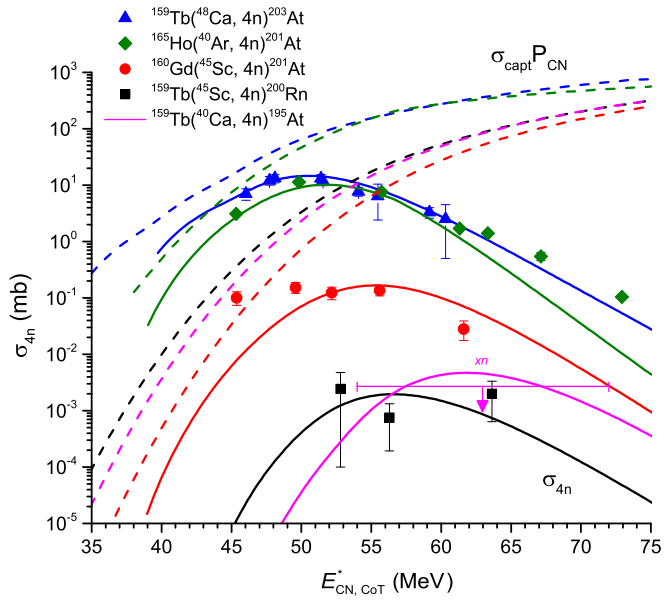

FIG. 3. (Color online) Comparison of measured and calculated cross sections for selected reactions. Symbols indicated measured data and solid lines indicate calculations according to the model described in Sec. IV. The ^{48}Ca-induced excitation function was reported in Ref. [5] and the ^{40}Ar-induced excitation function was reported in Ref. [4]. The arrow indicates the maximum measured cross section for xn EvRs in the ^{40}Ca + ^{159}Tb reaction [2], and the associated solid line indicates a calculation for the $4n$ channel only. Dashed lines are the product of the calculated capture cross section and the CN formation probability, $\sigma_{\mathrm{capt}}P_{\mathrm{CN}}$, and use the same color scheme as the solid lines. The other excitation functions are from the current work.

but do not provide a satisfactory description of the $p3n$ cross sections [see Fig. 2(b)]. The calculations are uniformly below the experimental data, suggesting that our model underestimates the probability of charged particle emission, even though the proton barrier has already been substantially reduced according to Eq. (13). The two most influential variables in the current calculations are B_p and a_p. Even by calculating B_p with Eq. (13), the values of Γ_p in the current model are small, and the $p3n$ excitation functions are underpredicted. It is possible that B_p is still too large and should be further reduced because it is the most likely explanation for the discrepancy. A small uncertainty in a_p can result in a large change in Γ_p, but a_p is calculated with the same well-established formalism as the neutron level density parameter a_n. The $4n$ excitation functions are well reproduced by the current model, suggesting that a_n (and therefore a_p) is trustworthy. Alternatively, an error in B_f could substantially affect both the calculated xn and pxn cross sections. In practice, the $4n$ data are well reproduced by the current model, suggesting that B_f is unlikely to be the source of error in the $p3n$ calculations.

Comparing Table III in the current work and Table II in Ref. [5] shows that xn cross sections in ^{45}Sc-induced reactions are two to three orders of magnitude smaller than ^{48}Ca-induced reactions on the same targets. Values of σ_{capt} and P_{CN} are

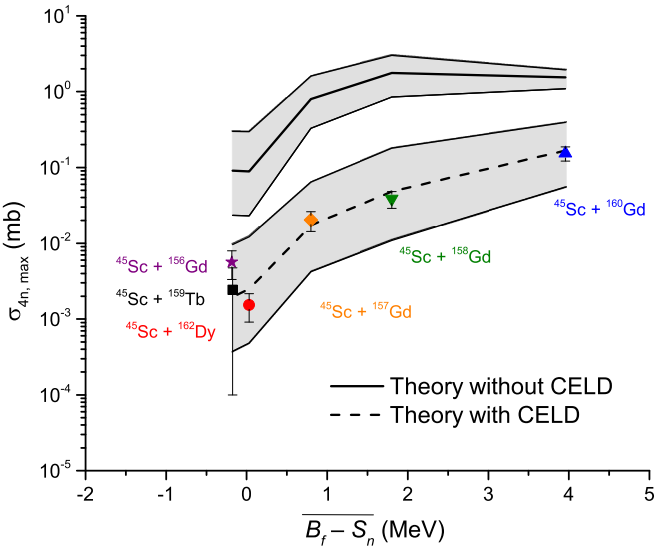

FIG. 4. (Color online) Comparison of model calculations described in Sec. IV without (solid line) and with (dashed line) CELD included, as a function of the average difference in fission barrier and neutron separation energy during the deexcitation cascade. Symbols indicate maximum experimental $4n$ cross sections. The shaded regions indicate the effect of changing the fission barrier by ±0.5 MeV.

similar for all of the reaction systems, so $W_{\rm sur}$ is the only term in Eq. (2) capable of producing differences of large orders of magnitude. Qualitatively, Oganessian and Utyonkov have reported that

$$W_{\rm sur} \propto \prod_{j=1}^{x} \exp\left[(B_f - S_n)/T\right]_j \qquad (21)$$

for xn reactions (see Eq. (3) in Ref. [17]). This leads to the rough approximation that

$$W_{\rm sur} \propto \{\exp[(\overline{B_f - S_n})/T]\}^x, \qquad (22)$$

where $\overline{B_f - S_n}$ is the average difference in fission barrier and neutron separation energy in each step of the deexcitation cascade. Values of $\overline{B_f - S_n}$ for the reaction systems studied in the current work are given in Table I. ^{45}Sc has four fewer neutrons than ^{48}Ca does, so compound nuclei produced by fusion with ^{45}Sc projectiles are much more neutron deficient. This leads to increased fissility caused by reduced B_f and increased S_n, both of which negatively impact $W_{\rm sur}$ in an exponential way. This phenomenon is illustrated in Fig. 4, which shows the peak $4n$ cross sections for the reactions studied in the current work as a function of $\overline{B_f - S_n}$. As the neutron number of the target decreases (as in the Gd target series), the values of $\overline{B_f - S_n}$ decrease while B_p remains approximately constant for all nuclei. Additionally, changing the target from ^{160}Gd to ^{162}Dy reduces $\overline{B_f - S_n}$ by ≈4 MeV but changes the peak $4n$ cross section by two orders of magnitude. These data suggest that maximizing $\overline{B_f - S_n}$ is critical to maximizing $W_{\rm sur}$ and $\sigma_{\rm EvR}$. Additionally, B_f has an estimated accuracy of ±0.5 MeV [52] (shown by the gray bands in Fig. 4), and this error is sufficient to change the calculated cross section by over one order of magnitude.

CELD also appears to have a substantial impact on $W_{\rm sur}$. Calculations with and without the inclusion of CELD are shown in Fig. 4 for $4n$ reactions. For *spherical* nuclei, which have $K_{\rm rot} = 1$, the level density at the deformed fission saddle is greatly enhanced compared to the ground state. CELD is thus expected to have the greatest effect near the spherical closed shells. In the current work, the inclusion of CELD reduces the calculated cross sections by approximately two orders of magnitude, and a similar decrease will be reported in a future publication for ^{50}Ti-induced reactions. Our previous work described the production of CN near the $N = 126$ closed shell and suggested that CELD *is* necessary to reproduce the experimental data [5]. This interpretation was consistent with previous reports discussing the influence of collective effects on reaction products near the $N = 126$ shell induced by ^{40}Ar [4], ^{48}Ca [3], and fragmentation of ^{238}U [59]. It should be noted, however, that Siwek-Wilczyńska *et al.* calculated each decay width independently for the ^{16}O + ^{208}Pb reaction and concluded that CELD is *not* necessary to reproduce data *away* from the $N = 126$ shell [13], although the reaction products in that system are substantially more neutron-rich than the products in the current work.

In these same works [3,4,59], the authors also discussed the lack of evidence for increased survival against fission even though the reaction products have substantial shell stabilizations. The products in the current work are relatively neutron deficient (see Table I), but still have CN shell corrections of ≈2–5 MeV [45]. These should increase the fission barrier and the EvR cross section, but the CN neutron separation energies are very high (all but one have $S_n >$ 9 MeV; see Table I) and largely counteract this effect. Our data are consistent with the previous interpretations that proximity to the $N = 126$ shell does not lead to cross section enhancement.

Despite a recent prediction that the ^{248}Cm($^{45}Sc, xn$)$^{293-x}$117, $x = 2$–4 reactions could have cross sections as high as 2–4 pb [18] (comparable to ^{48}Ca-induced reactions), the experimental data in the current work suggest that the actual cross sections would likely be much smaller due to reduced survival of the CN and competition with pxn exit channels. Due to the relative neutron deficiency of ^{45}Sc, the use of ^{45}Sc for production of SHEs in hot fusion reactions does not appear promising. These expectations are supported by calculations by Ohta and Aritomo, which predict substantial decreases in xn cross sections for ^{45}Sc-induced reactions compared to ^{48}Ca-induced reactions [19]. Instead, the current work advocates even-Z projectiles beyond ^{48}Ca in campaigns to synthesize the next superheavy element.

VI. CONCLUSIONS

Excitation functions for hot fusion reactions of ^{45}Sc projectiles reacting with lanthanide targets are reported for the first time. Cross sections are 2–3 orders of magnitude smaller than ^{48}Ca-induced reactions on the same targets, and the pxn

exit channels were competitive with the xn exit channels. A simple theoretical model was employed to understand the $4n$ and $p3n$ excitation functions. The primary factor behind the large reduction in the cross sections is a substantial decrease in the survival of the CN caused by its relative neutron deficiency. This is a result of the low values of $\overline{B_f - S_n}$ and the influence of CELD. The inclusion of CELD appears critical to accurately reproducing the experimental cross sections, as estimates without CELD were too large by approximately two orders of magnitude. Additionally, the barriers for proton emission had to be reduced by 40% compared to *a priori* estimates to obtain reasonable agreement with the data. The angular momentum of the CN had to be reduced by ∼60% and limited to $l_{\mathrm{CN}} \leqslant 25\hbar$. The expected increase in cross section due to shell corrections of a few MeV was not observed. Taken together, the results indicate that ^{45}Sc shows little promise for producing SHEs in fusion reactions with actinide targets due its relative neutron deficiency compared to ^{48}Ca or ^{50}Ti.

ACKNOWLEDGMENTS

The authors would like to thank the accelerator group and technical staff of the Cyclotron Institute for delivering the beams of ^{45}Sc. We also thank the Heavy Elements Group at Lawrence Berkeley National Laboratory for providing the ^{162}Dy target used in these experiments. Finally, we thank the machine shop of the Chemistry Department at Texas A&M University for fabricating the target cells used to electrodeposit the $^{156-158,160}Gd_2O_3$ targets. This material is based upon work supported by the U.S. Department of Energy, Office of Science, Office of Nuclear Physics under Grants No. DE-FG02-93ER40773, No. DE-FG02-12ER41869/DE-SC0008126, and No. DE-FG07-05ID14692/MUSC09-100. Additionally, this work was supported by the Robert A. Welch Foundation under Grant No. A-1710, the Texas A&M University College of Science, and the U.S. National Science Foundation under Grant No. PHY-1004780.

[1] A. N. Andreyev *et al.*, Phys. Rev. C **72**, 014612 (2005).
[2] A. N. Andreev *et al.*, Sov. J. Nucl. Phys, **52**, 412 (1990).
[3] C.-C. Sahm, H.-G. Clerc, K.-H. Schmidt, W. Reisdorf, P. Armbruster, F. P. Hessberger, J. G. Keller, G. Münzenberg, and D. Vermeulen, Nucl. Phys. A **441**, 316 (1985).
[4] D. Vermeulen, H.-G. Clerc, C.-C. Sahm, K.-H. Schmidt, J. G. Keller, G. Munzenberg, and W. Reisdorf, Z. Phys. A **318**, 157 (1984).
[5] D. A. Mayorov, T. A. Werke, M. C. Alfonso, M. E. Bennett, and C. M. Folden III, Phys. Rev. C **90**, 024602 (2014).
[6] W. Reisdorf, Z. Phys. A **300**, 227 (1981).
[7] A. Gavron, Phys. Rev. C **21**, 230 (1980).
[8] F. Pühlhofer, Nucl. Phys. A **280**, 267 (1977).
[9] V. I. Zagrebaev, Y. Aritomo, M. G. Itkis, Yu. Ts. Oganessian, and M. Ohta, Phys. Rev. C **65**, 014607 (2001).
[10] N. V. Antonenko, E. A. Cherepanov, A. K. Nasirov, V. P. Permjakov, and V. V. Volkov, Phys. Lett. B **319**, 425 (1993).
[11] G. G. Adamian, N. V. Antonenko, W. Scheid, and V. V. Volkov, Nucl. Phys. A **627**, 361 (1997).
[12] W. J. Świątecki, K. Siwek-Wilczyńska, and J. Wilczyński, Phys. Rev. C **71**, 014602 (2005).
[13] K. Siwek-Wilczyńska, I. Skwira, and J. Wilczyński, Phys. Rev. C **72**, 034605 (2005).
[14] A. R. Junghans, M. de Jong, H. G. Clerc, A. V. Ignatyuk, G. A. Kudyaev, and K. H. Schmidt, Nucl. Phys. A **629**, 635 (1998).
[15] H. A. Kramers, Physica **VII**, 284 (1940).
[16] C. M. Folden III, D. A. Mayorov, T. A. Werke, M. C. Alfonso, M. E. Bennett, and M. J. DeVanzo, J. Phys.: Conf. Ser. **420**, 012007 (2013).
[17] Yu. Ts. Oganessian and V. K. Utyonkov, Rep. Prog. Phys. **78**, 036301 (2015).
[18] W. J. Zhao, Y. Q. Zhang, H. L. Wang, L. T. Song, and L. L. Li, Chin. Phys. C **34**, 1609 (2010).
[19] M. Ohta and Y. Aritomo, Phys. At. Nuclei **66**, 1026 (2003).
[20] W. Parker and R. Falk, Nucl. Instrum. Methods **16**, 355 (1962).
[21] W. Parker, H. Bildstein, N. Getoff, H. Fischer-Colbrie, and H. Regal, Nucl. Instrum. Methods **26**, 61 (1964).
[22] R. E. Tribble, R. H. Burch, and C. A. Gagliardi, Nucl. Instrum. Methods. Phys. Res., Sect. A **285**, 441 (1989).
[23] R. E. Tribble, C. A. Gagliardi, and W. Liu, Nucl. Instrum. Methods. Phys. Res., Sect. B **56/57**, 956 (1991).
[24] C. M. Folden III *et al.*, Nucl. Instrum. Methods A **678**, 1 (2012).
[25] J. F. Ziegler, M. D. Ziegler, and J. P. Biersack, Nucl. Instrum. Methods. Phys. Res., Sect. B **268**, 1818 (2010).
[26] J. F. Ziegler *et al.*, *The Stopping and Range of Ions in Solids* (Pergamon, New York, 1984).
[27] O. Tarasov and D. Bazin, Nucl. Instrum. Methods. Phys. Res., Sect. B **266**, 4657 (2008).
[28] G. Schiwietz and P. L. Grande, Nucl. Instrum. Methods. Phys. Res., Sect. B **175**, 125 (2001).
[29] S. Nath, Comput. Phys. Commun.**179**, 492 (2008).
[30] S. Nath, Comput. Phys. Commun.**180**, 2392 (2009).
[31] National Nuclear Data Center; available at http://www.nndc.bnl.gov/chart/.
[32] D. C. Radford, RADWARE software package, available at http://radware.phy.ornl.gov.
[33] K.-H. Schmidt, C.-C. Sahm, K. Pielenz, and H.-G. Clerc, Z. Phys. A **316**, 19 (1984).
[34] A. C. Berriman, D. J. Hinde, M. Dasgupta, C. R. Morton, R. D. Butt, and J. O. Newton, Nature (London) **413**, 144 (2001).
[35] D. J. Hinde, M. Dasgupta, J. R. Leigh, J. P. Lestone, J. C. Mein, C. R. Morton, J. O. Newton, and H. Timmers, Phys. Rev. Lett. **74**, 1295 (1995).
[36] E. Prasad *et al.*, Phys. Rev. C **81**, 054608 (2010).
[37] C. Yadav *et al.*, Phys. Rev. C **86**, 034606 (2012).
[38] E. Williams *et al.*, Phys. Rev. C **88**, 034611 (2013).
[39] G. N. Knyazheva *et al.*, Phys. Rev. C **75**, 064602 (2007).
[40] R. N. Sagaidak *et al.*, Phys. Rev. C **68**, 014603 (2003).
[41] K. Siwek-Wilczyńska, A. Borowiec, I. Skwira-Chalot, and J. Wilczyński, Int. J. Mod. Phys. E **17**, 12 (2008).
[42] R. Yanez, W. Loveland, J. S. Barrett, L. Yao, B. B. Back, S. Zhu, and T. L. Khoo, Phys. Rev. C **88**, 014606 (2013).
[43] J. D. Jackson, Can. J. Phys. **34**, 767 (1956).
[44] V. Weisskopf, Phys. Rev. **52**, 295 (1937).
[45] P. Möller, J. R. Nix, W. D. Myers, and W. J. Świątecki, At. Data Nucl. Data Tables **59**, 185 (1995).
[46] W. D. Myers and W. J. Świątecki, Ann. Phys. (NY) **84**, 186 (1974).

[47] A. V. Ignatyuk, G. N. Smirenkin, and A. S. Tishin, Sov. J. Nucl. Phys. **21**, 255 (1975).
[48] L. G. Moretto, Phys. Lett. B **40**, 185 (1972).
[49] L. G. Moretto, Nucl. Phys. A **247**, 211 (1975).
[50] W. E. Parker *et al.*, Phys. Rev. C **44**, 774 (1991).
[51] A. J. Sierk, Phys. Rev. C **33**, 2039 (1986).
[52] A. J. Sierk, computer code FISROT, available at https://www-nds.iaea.org/RIPL-3/fission/fis-barrier-liquiddrop.for.
[53] K. Hagino, N. Rowley, and A. T. Kruppa, Comput. Phys. Commun. **123**, 143 (1999).
[54] G. Henning *et al.*, Phys. Rev. Lett. **113**, 262505 (2014).
[55] F. Plasil and R. L. Ferguson, in *Proceedings of the International Symposium of Physics and Chemistry of Fission, Jülich, 1979* (IAEA, Vienna, 1980), p. 521.
[56] J. Cabrera *et al.*, Phys. Rev. C **68**, 034613 (2003).
[57] W. Loveland, D. J. Morrissey, and G. T. Seaborg, *Modern Nuclear Chemistry* (John Wiley & Sons, Hoboken, New Jersey, 2006).
[58] S. Cohen and W. J. Świątecki, Ann. Phys. (NY) **22**, 406 (1963).
[59] A. Heinz *et al.*, Nucl. Phys. A **713**, 3 (2003).